

Article

# Bifurcation Stability Analysis of the Synchronverter in a Microgrid

Juan Segundo Ramírez , Josué Hernández Ramírez, Nancy Visairo Cruz  and Rafael Peña Gallardo \* 

Facultad de Ingeniería, Universidad Autónoma de San Luis Potosí, San Luis Potosí 78290, Mexico

\* Correspondence: rafael.pena@uaslp.mx; Tel.: +52-4448262330

**Abstract:** Synchronized converters are being studied as a viable alternative to address the transition from synchronous generation to power-electronics-based generation systems. One of the important features that make the synchronous generator an unrivaled alternative for power generation is its stability properties and inherent inertial response. This work presents a stability analysis of a synchronverter-based system conducted through the bifurcation theory to expose its stability regions in a grid-connected configuration with an aggregate load model conformed by a ZIP model and an induction motor model. One and two-parameter bifurcation diagrams on the gain, load, and Thévenin equivalent plane are computed and analyzed. All the results confirm the strong stability properties of the synchronverter. Some relevant findings are that the reduction in a droop gain or time constant results in Hopf bifurcations and inertia reduction, but the increase in the time constant leads to decoupling between the reactive and active power loops. It is also found that the increment of a specific time constant ( $\tau_f > 0.02$  s) increases the stability region on the droop gains plane to all positive values. It is also found that a low lagging power factor reduces the feasible operating and stable operating regions. For a lagging power factor above 0.755, subcritical Hopf bifurcation disappears, and also, the feasible operating solution overlaps the stability region. Finally, it is also found how the Thévenin equivalent affects the stability and that the stability boundary is delimited by Hopf bifurcations. The bifurcation diagrams are numerically computed using XPP Auto software.

**Keywords:** bifurcation; eigenvalues; inertia; AC microgrid; planning methods; stability; synchronverter



**Citation:** Segundo Ramírez, J.; Hernández Ramírez, J.; Visairo Cruz, N.; Peña Gallardo, R. Bifurcation Stability Analysis of the Synchronverter in a Microgrid. *Energies* **2022**, *15*, 7992. <https://doi.org/10.3390/en15217992>

Academic Editors: Juan C. Vasquez, Gibran David Agundis Tinajero and Yajuan Guan

Received: 23 September 2022

Accepted: 10 October 2022

Published: 27 October 2022

**Publisher's Note:** MDPI stays neutral with regard to jurisdictional claims in published maps and institutional affiliations.



**Copyright:** © 2022 by the authors. Licensee MDPI, Basel, Switzerland. This article is an open access article distributed under the terms and conditions of the Creative Commons Attribution (CC BY) license (<https://creativecommons.org/licenses/by/4.0/>).

## 1. Introduction

Virtual synchronous generators (VSG) are inverters that use a control law that allows them to emulate, to a greater or lesser extent, the behavior of conventional synchronous generators (SG). The synchronverter proposed by Zhong and Weiss in [1,2] is a VSG topology that uses a proper control law that imitates the dynamics of the SG. Therefore, this topology makes the interoperation between the SG and inverters possible, allowing the power system to not present major changes in its operation or in the controllers and studies currently used [3].

One advantage of the synchronverter regarding SG is that some of its parameters, such as inertia and damping coefficient, can be changed online, changing the dynamics of the system accordingly. This can be observed in [4], where a parameter design for this synchronverter is presented. However, the variation of these parameters can lead the system to an unstable state causing unexpected behaviors. Therefore, to guarantee the reliable operation of the power systems that have these grid-connected synchronverters, it is necessary to conduct a stability analysis to determine how the parameters affect their stability.

Several theories and methods can be used to perform a stability analysis of power electronic-based power systems, such as small-signal [5,6], robust stability [7], transient stability [5,8], bifurcation analysis [9–11], and impedance methods [12,13], among others.

The bifurcation analysis is the best-suited method to analyze the stability of the nonlinear systems subjected to quasistatic parameter changes [14,15]. The bifurcation theory allows for determining the stability regions in the parameter space [10,11]. The stability region boundary can be computed using continuation methods to effectively track the roots of the dynamical system against parameter variations. These stable regions reveal the set of system parameters for which the system exhibits stable behavior. Although this information refers to the stability of the small signal, it is valuable, and this type of stability is essential for the correct operation of the system.

Previous work has presented a bifurcation analysis for synchronverter-based systems where saddle-node and Hopf bifurcations were found as a result of the variation of the droop coefficients [9], but small-signal stability has also been used to assess the effect of grid impedance variation on the stability of synchronverters [16,17]. Other works use frequency domain analyses, such as structured singular value analysis [18] and impedance-based methods [12], to appreciate the variation of parameters of the synchronverter with frequency dependence and observe its stability. In [10], the authors present a deep bifurcation analysis of an islanded microgrid with a ZIP and a nonlinear load represented by an induction motor model, as in [19], for voltage stability. Recently, the stability boundary analysis of islanded droop-based microgrids using an autonomous shooting method is presented in [20], showing that instability is caused by supercritical Neimark–Sacker bifurcations.

This paper performs the stability analysis based on the bifurcation theory of a grid-connected synchronverter with local ZIP and nonlinear loads. The analyses are conducted in one and two parameters, considering the variation of the control gains, inertia, load level, and grid equivalent. All the bifurcation diagrams are numerically computed with the XPP Auto program built-in continuation method [21]. Unlike previous works, this article presents stability boundary to qualitatively and quantitatively identify the relationship and dependency between the main parameter of the synchronverter controllers and the characteristics of the network. This analysis can be extended and applied to other network topologies with several power electronic converters and loads to compute the stability limits and the parameter relationship that contribute to the enhancement of the system performance. Table 1 shows a comparison of the proposed work against some previous works in terms of particular salient features. All of these works are focused on stability and the synchronverter, except [10], but it presents a bifurcation analysis of a power electronic-based microgrid with nonlinear and ZIP load, as in the present work. The main research gap is the computation of the stability and feasible regions on the gain and Thevenin spaces. The proposed work presents a qualitative analysis of the different systems and control parameters that lead to smaller or larger stable regions.

**Table 1.** Stability analysis in previous works.

Features	[5]	[6]	[7]	[8]	[9]	[10]	[17]	[18]	Proposed
Synchronverter	✓	✓	✓	✓	✓		✓	✓	✓
Small-signal stability	✓	✓					✓	✓	✓
Transient stability	✓			✓					
Robust stability			✓						
Stability boundary						✓			✓
Solution type					✓	✓			✓
Stability region (gain space)						✓			✓
Stability region (Thevenin space)									✓
Experimental validations			✓		✓	✓	✓	✓	
Decoupling gains									✓
Feasible solution boundary									✓
Power-Hardware-in-the-loop validation			✓					✓	
Nonlinear-ZIP load						✓			✓

The rest of the paper is organized as follows. Section 2 presents the nonlinear model of the test system. The results of the bifurcation analysis of the synchronverter and the electrical parameters are presented in Section 3. Finally, Section 4 presents the conclusion of the presented work.

## 2. Synchronverter Modeling with a Nonlinear Load Connected to the Network

This section describes the modeling of the test system shown in Figure 1 and all its electrical elements. The models of each component are widely known in the literature but are briefly described here.

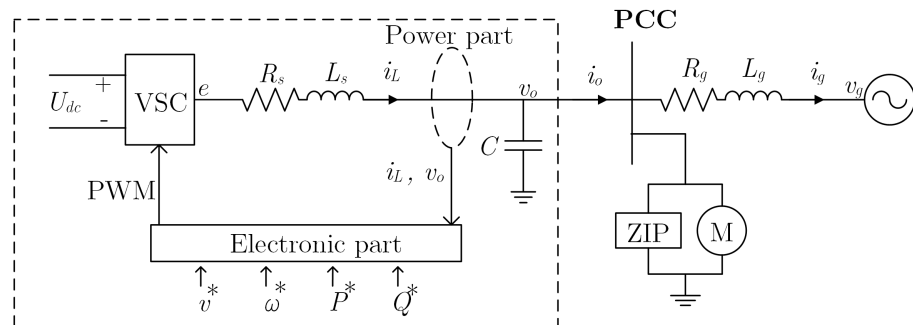


Figure 1. Grid-connected synchronverter.

### 2.1. Synchronverter Topology

#### 2.1.1. Operating Principle

The synchronverter was proposed by [1] as a generation unit that, thanks to its control law, can imitate the dynamics of the synchronous generator. This has a power part and an electronics part, as shown in Figures 1 and 2. The power part comprises a three-phase inverter and an RLC filter. The measurements of the output current of the filter  $i_L$  and the voltage in the capacitor  $v_o$  are sent to the electronic part to generate the switching signal of the VSC, thus regulating the output voltage of the inverter  $e$ . The test system of Figure 1 is based on [10,19,22] and has been widely used for stability analysis.

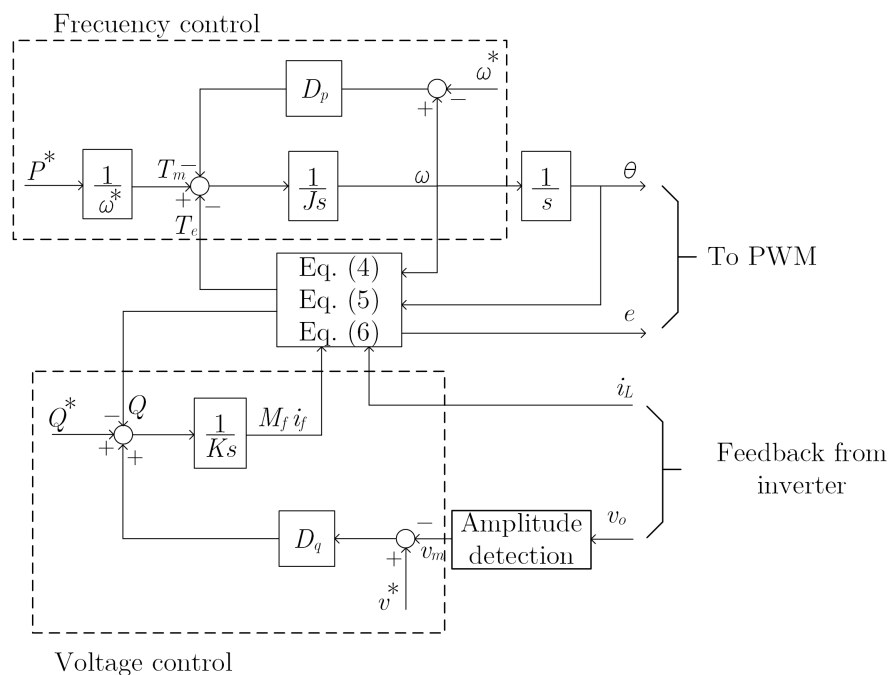


Figure 2. Electronic part of the synchronverter [1].

The electronic part of the synchronverter comprises some basic equations that capture the dynamics of the synchronous generator and two controllers; one for active power regulation and the other for reactive power regulation, as shown in Figure 2. Next, the mathematical model of the synchronverter proposed by [1] is briefly described.

The equations that emulate the mechanical part of the synchronverter are [1]:

$$J\dot{\omega} = \frac{P^*}{\omega^*} - T_e - D_p(\omega^* - \omega) \tag{1}$$

$$\dot{\theta} = \omega \tag{2}$$

$$J = \tau_f D_p \tag{3}$$

$$T_e = M_f i_f \langle i_L, \widetilde{\sin \theta} \rangle \tag{4}$$

where  $J$  is the combined moment of inertia of the generator and is prime-mover,  $D_p$  is the frequency-drooping coefficient,  $T_e$  is the electrical torque,  $i_L$  is the inverter output current,  $\omega$  is the angular speed in rad/s,  $\omega^*$  is the reference angular speed in rad/s,  $\theta$  is the angle of the imaginary rotor in rad,  $P^*$  is the power reference, and  $\tau_f$  is the time constant of the frequency-droop loop. In addition,  $M_f$  and  $i_f$  denote the virtual mutual inductance and the imaginary rotor excitation current, respectively.

On the other hand, the voltage inverter  $e$ , the active power  $P$ , and the reactive power  $Q$  are calculated with the following equations:

$$e = \dot{\theta} M_f i_f \widetilde{\sin \theta} \tag{5}$$

$$P = \dot{\theta} M_f i_f \langle i_L, \widetilde{\sin \theta} \rangle \tag{6}$$

$$Q = -\dot{\theta} M_f i_f \langle i_L, \widetilde{\cos \theta} \rangle$$

$D_q$  is the voltage-drooping gain,  $\tau_v$  is the time constant of the voltage loop,  $K$  is another coefficient of inertia related to the gain  $D_q$ ,  $v_m$  is the amplitude of the synchronverter output voltage, and  $v^*$  is the amplitude of the reference voltage. More details of the synchronverter model can be found in the original reference [1]. The vectors  $\widetilde{\cos \theta}$  and  $\widetilde{\sin \theta}$  are [1]:

$$\widetilde{\cos \theta} = \begin{bmatrix} \cos \theta \\ \cos\left(\theta - \frac{2\pi}{3}\right) \\ \cos\left(\theta - \frac{4\pi}{3}\right) \end{bmatrix} \quad \widetilde{\sin \theta} = \begin{bmatrix} \sin \theta \\ \sin\left(\theta - \frac{2\pi}{3}\right) \\ \sin\left(\theta - \frac{4\pi}{3}\right) \end{bmatrix} \tag{7}$$

### 2.1.2. Synchronverter Model

The synchronverter frame is considered the common frame of reference. All other frames are referred to as this common frame of reference using the transformation technique shown in [23], which is represented in Figure 3 and is defined by (8).

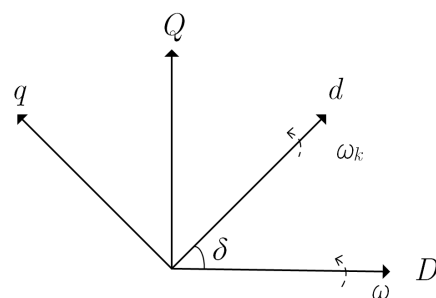


Figure 3. Relationship between the reference frame [23].

$$\begin{bmatrix} F_D \\ F_Q \end{bmatrix} = \begin{bmatrix} \cos \delta & -\sin \delta \\ \sin \delta & \cos \delta \end{bmatrix} \begin{bmatrix} f_d \\ f_q \end{bmatrix} \quad (8)$$

where  $\omega$  represents the virtual angular frequency of the synchronverter,  $\omega_k$  is the angular frequency of the electrical component to refer to,  $\delta$  is the difference between the phase angle of the frame  $dq$  and the common frame of reference  $DQ$  of the synchronverter.  $F_D$  and  $F_Q$  represent the electrical quantities in the common reference frame translated from their original frame  $f_d$  and  $f_q$ .

Therefore,  $\delta$  can be expressed as [1]:

$$\frac{d\delta}{dt} = \omega_k - \omega \quad (9)$$

Then, using the  $DQ$  transform, Equations (4)–(6) can be rewritten in the common frame of reference as [1]:

$$e_D = \omega M_f i_f \quad (10)$$

$$T_e = \frac{3}{2} i_{LD} M_f i_f \quad (11)$$

$$Q = -\frac{3}{2} \omega i_{LQ} M_f i_f \quad (12)$$

Whereas the state equations for the RLC filter in the  $DQ$  frame can be described as follows [1]:

$$L_s \dot{i}_{LD} = e_D - v_{oD} - i_{LD} R_s + i_{LQ} \omega L_s \quad (13)$$

$$L_s \dot{i}_{LQ} = e_Q - v_{oQ} - i_{LQ} R_s + i_{LD} \omega L_s \quad (14)$$

$$C \dot{v}_{oD} = i_{LD} - i_{oD} + v_{oQ} \omega C \quad (15)$$

$$C \dot{v}_{oQ} = i_{LQ} - i_{oQ} + v_{oD} \omega C \quad (16)$$

Finally, by adding the three control equations shown in Figure 2, the synchronverter model is complete and is represented by Equations (9)–(20) [1].

$$J \dot{\omega} = \frac{P^*}{\omega^*} - T_e - D_p (\omega^* - \omega) \quad (17)$$

$$\dot{\theta} = \omega \quad (18)$$

$$M_f \dot{i}_f = \frac{1}{K} [Q^* + D_q (v^* - v_m) - Q] \quad (19)$$

$$K = \tau_v \omega D_q \quad (20)$$

### 2.1.3. Thévenin Equivalent Model

Using the transformation technique seen in (8), the network voltage referred to as the common reference frame is expressed by Equations (21) and (22) [1]:

$$u_{gD} = V_p \cos(\delta) \quad (21)$$

$$u_{gQ} = V_p \sin(\delta) \quad (22)$$

On the other hand, the equation of currents of the short-line equivalent model is:

$$L_g \dot{i}_{gD} = v_{oD} - v_{gD} - i_{gD} R_g + i_{gQ} \omega L_g \quad (23)$$

$$L_g \dot{i}_{gQ} = v_{oQ} - v_{gQ} - i_{gQ} R_g - i_{gD} \omega L_g \quad (24)$$

## 2.2. Induction Motor

In this research work, the squirrel cage induction motor (IM) is selected as a nonlinear dynamic load [24]. The flux equations of the stator  $\psi_s$  and rotor  $\psi_r$  of the induction motor model can be written as [25]:

$$\psi_{sQ} = L_s i_{sQ} + L_m i_{rQ} \quad (25)$$

$$\psi_{sD} = L_s i_{sD} + L_m i_{rD} \quad (26)$$

$$\psi_{rQ} = L_r i_{rQ} + L_m i_{sQ} \quad (27)$$

$$\psi_{rD} = L_r i_{rD} + L_m i_{sD} \quad (28)$$

$L_m$  is the magnetization inductance, and  $L_s$  and  $L_r$  are the inductances of the stator and rotor, respectively.

The IM voltage equations are described as [25]:

$$v_{sQ} = R_s i_{sQ} + \dot{\psi}_{sQ} + \omega \psi_{sD} \quad (29)$$

$$v_{sD} = R_s i_{sD} + \dot{\psi}_{sD} + \omega \psi_{sQ} \quad (30)$$

$$0 = R_r i_{rQ} + \dot{\psi}_{rQ} + (\omega - \omega_{em}) \psi_{rD} \quad (31)$$

$$0 = R_r i_{rD} + \dot{\psi}_{rD} - (\omega - \omega_{em}) \psi_{rQ} \quad (32)$$

where  $R_s$  and  $R_r$  are the stator and rotor resistances, respectively.  $\omega$  is the angular velocity of the common reference frame, and  $\omega_{em}$  is the electrical angular velocity of the motor. The previous equations describe the model of the electrical part of the IM. The mechanical part is governed by the oscillation equation [25]:

$$\dot{\omega}_{mm} = \frac{1}{J_m} (T_{em} - D_m \omega_{mm} - T_{mm}) \quad (33)$$

$$\dot{\theta}_{mm} = \omega_{mm} \quad (34)$$

$$\omega_{em} = \omega_m p \quad (35)$$

where  $J_m$  is the moment of inertia of the motor,  $\omega_{mm}$  is the mechanical angular speed of the motor,  $p$  is the number of pole pairs,  $D_m$  is the damping constant,  $T_{mm}$  is the mechanical torque, and  $T_{em}$  is the electromagnetic torque, which is described by [25]:

$$T_{em} = 1.5p (\psi_{sD} i_{sQ} - \psi_{sQ} i_{sD}) \quad (36)$$

## 2.3. ZIP Load Model

This model represents the relationship between the magnitude of the voltage and the power in a polynomial equation [26]. The polynomial model for active power and reactive power is given by:

$$P_{ZIP} = P_0 \left( a_1 \frac{U_b^2}{U_0^2} + a_2 \frac{U_b}{U_0} + a_3 \right) \quad (37)$$

$$Q_{ZIP} = Q_0 \left( b_1 \frac{U_b^2}{U_0^2} + b_2 \frac{U_b}{U_0} + b_3 \right)$$

where  $P_0$  and  $Q_0$  are the active and reactive nominal power, respectively, at nominal voltage conditions  $U_0$ .  $U_b$  defines the actual bus voltage magnitude.  $a_1$  and  $b_1$ ,  $a_2$  and  $b_2$ ,  $a_3$  and  $b_3$  are the weights of constant impedance load, constant current load, and constant power load, respectively.

This model can also be represented as a variant conductance  $G_{ZIP}$  and a susceptance  $B_{ZIP}$  in parallel [9]. This susceptance and conductance are described by the following equations:

$$\begin{aligned} G_{ZIP} &= P_0 \left( \frac{a_1}{U_0^2} + \frac{a_2}{U_0 U_b} + \frac{a_3}{U_b^2} \right) \\ B_{ZIP} &= -Q_0 \left( \frac{b_1}{U_0^2} + \frac{b_2}{U_0 U_b} + \frac{b_3}{U_b^2} \right) \end{aligned} \quad (38)$$

The ZIP load current equations can be presented in the common frame of reference as:

$$\begin{aligned} \tau i_{PD} &= G_{ZIP} u_{oD} - i_{PD}, \tau i_{PQ} = G_{ZIP} u_{oQ} - i_{PQ} \\ \tau i_{QD} &= -B_{ZIP} u_{oQ} - i_{QD}, \tau i_{QQ} = B_{ZIP} u_{oD} - i_{QQ} \end{aligned} \quad (39)$$

where  $\tau$  is the time constant of the ZIP load model.

The power factor  $PF$  can be included in this load model, using an equation where the reference reactive power  $Q_0$  is a function of the reference active power  $P_0$  and  $PF$ . This equation is described by:

$$Q_0 = \pm P_0 \left( \sqrt{\frac{1}{PF^2} - 1} \right) \quad (40)$$

The sign depends on whether the power factor is lagging (+) or leading (-).

### 3. Bifurcation Analysis

#### 3.1. Synchronverter

In this section, the XPP Auto program built-in continuation method is used to compute the stability regions of the test system shown in Figure 1. The system parameters are given in Table 2, and the initial operating point for branch analysis is shown in Table 3.

**Table 2.** Synchronverter-based system parameters.

Parameter	Value	Parameter	Value
$p$	2	$J_m$	0.4 kg · m <sup>2</sup>
$R_s$	0.0996 Ω	$L_s$	0.0103 H
$R_r$	0.0583 Ω	$L_r$	0.0103 H
$L_m$	9.415 mH	$D_{pm}$	0.02187
$T_{mm}$	250 N · m	$C$	1.56 mF
$L_g$	0.565 mH	$R_g$	0.021 Ω
$L_s$	0.57 mH	$R_s$	0.042 Ω
$P^*$	80 kW	$Q^*$	0 kVAR
$v^*$	375.58842 V	$V_p$	375.588 V
$\omega^*$	376.99 rad/s	$\omega_{grid}$	376.99 rad/s
$D_q$	5324.97	$D_p$	140.7
$\tau_f$	0.002 s	$\tau_v$	0.02 s
$P_0$	50 kW	$P_{base}$	100 kW
$a_1, b_1$	0.2	$a_2, b_2$	0.3
$a_3, b_3$	0.5	$U_0$	460 V
$PF$	0.61 (lagging)	$\tau$	0.01 s

**Table 3.** Equilibrium point for the synchronverter test case.

Variable	Value	Variable	Value
$i_{LD}$	139.8225 A	$i_{LQ}$	-12.2405 A
$v_{oD}$	373.1030 V	$v_{oQ}$	-29.4594 V
$i_{gD}$	-42.7562 A	$i_{gQ}$	4.8043 A
$\omega_{mm}$	181.8135 rad/s	$\omega$	376.9911 rad/s
$\psi_{sD}$	-0.0363 wb	$\psi_{sQ}$	-0.9492 wb
$\psi_{rD}$	-0.3178 wb	$\psi_{rQ}$	-0.7483 wb
$i_{PD}$	17.713 A	$i_{PQ}$	-1.4 A
$i_{QD}$	-6.02 A	$i_{QQ}$	-76.12 A
$\delta$	-0.0546 rad	$M_f I_f$	1.0122 HA

### 3.1.1. Bifurcation Analysis in the Gain Space $D_p$ - $D_q$

The first parameter that was selected to vary was  $D_p$ , but no bifurcation was observed from its initial value of 140.7 to 10,000. On the other hand, the resulting bifurcation diagram from varying  $D_q$  is shown in Figure 4. In the unstable regions, the system presents two types of bifurcations; a stable Hopf bifurcation (SHB) in  $D_q = 601.1$ , and a torus bifurcation (TRB) in  $D_q = 383.5$ . At the SHB, two branches of stable periodic solutions are born, which causes the variables of the system to oscillate. These branches of stable periodic solutions change stability at the TRB point. In these stable periodic solutions, the system presents an oscillatory behavior, for example, when the gain is decreased to a value of  $D_q = 571$ , the system variables begin to oscillate with a frequency of approximately 62 Hz instead of having a constant value; this is shown in Figure 5. The bifurcation diagram shows that for  $D_q < 601.1$ , the system is unstable since, below this bifurcation value, periodic solutions and even lower values emerge ( $D_q < 383.5$ ), and thus, this unstable periodic solution evolves into a quasiperiodic solution. This behavior demonstrates that, for the test systems, a sign of loss of stability is the apparition of sustained oscillation on the amplitude of the electric and control variables.

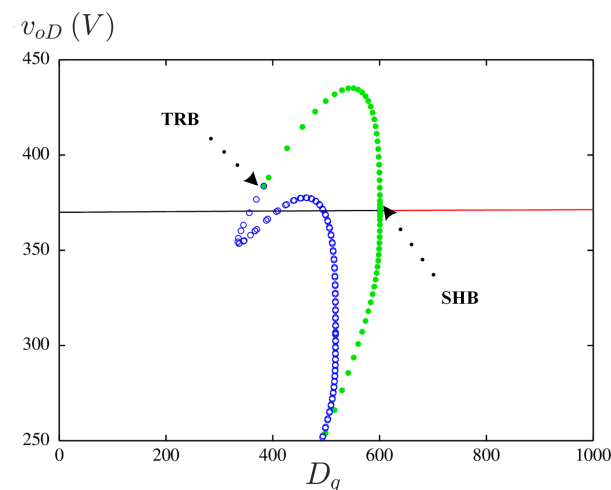


**Figure 4.** Bifurcation diagram by varying  $D_q$ : stable solutions in red, unstable solutions in black, stable periodic solutions in green, and unstable periodic solutions in blue.

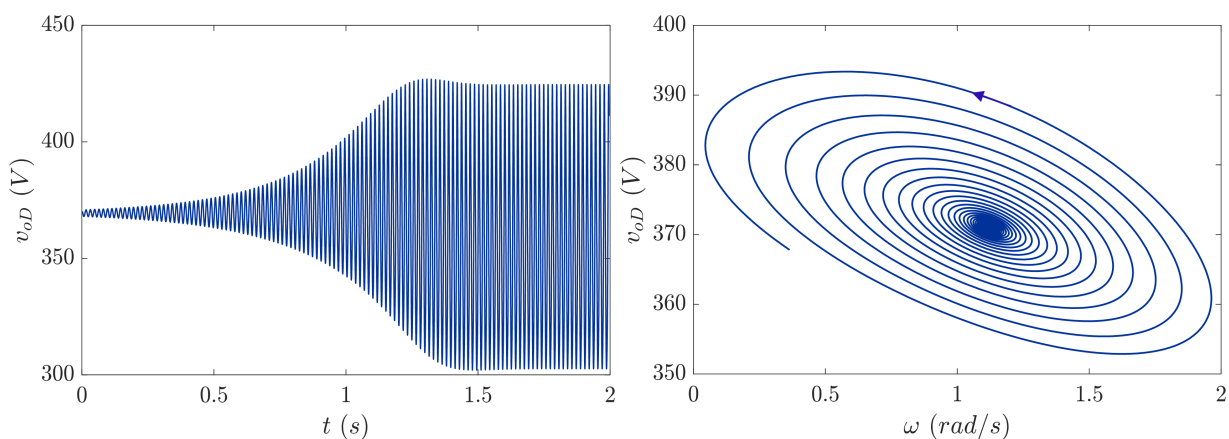


**Figure 5.** Periodic oscillations due to SHB bifurcation in  $D_q = 571$ .

The behavior of the TRB can be explained as follows. If the system suffers a disturbance and the values of the variables fall at the point where the bifurcation parameter is greater than the bifurcation point, for example, at  $D_q = 390$ , the system oscillates at over one frequency until it stabilizes in a periodic orbit (Figure 6). If the bifurcation parameter is less

than the bifurcation point, for example,  $D_q = 380$ , it oscillates with increasing amplitude (Figure 7).

The eigenvalues are shown in Table 4, and Figure 8 presents the harmonic spectrum of the corresponding quasiperiodic solution to exhibit the frequency components. The results show that besides the oscillation frequency of 62 Hz captured by the eigenvalues, there is a slower oscillation component at 3.25 Hz and two others with higher frequencies at 123 Hz and 185 Hz. The slowest and highest oscillation frequencies are not observed in the eigenvalues, but this can be attributed to the fact that these components are nonlinear and therefore are not captured by the eigenvalues.

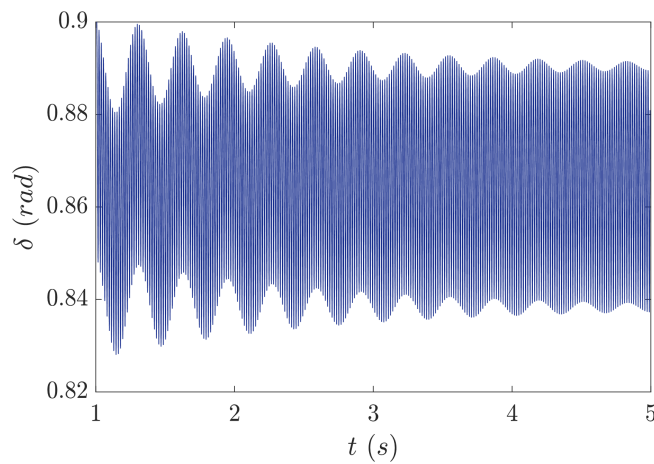


Figure 6. Bounded oscillations with two frequencies due to the torus bifurcation in  $D_q = 390$ .

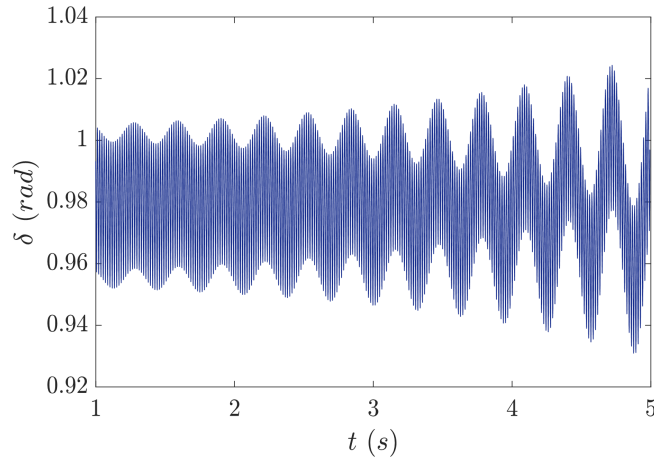
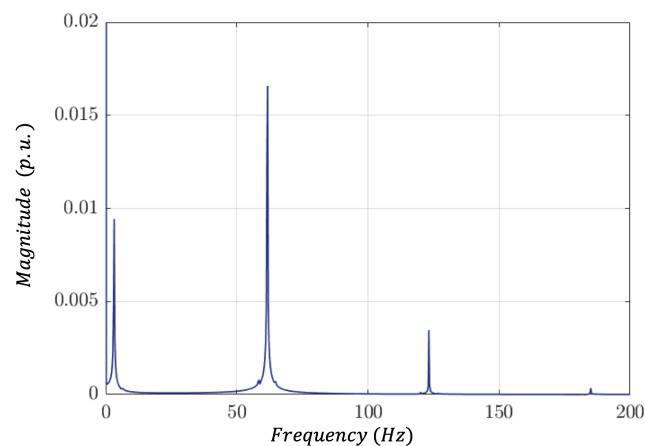


Figure 7. Increasing oscillations due to the torus bifurcation in  $D_q = 380$ .

Table 4. Eigenvalues that occur at the torus bifurcation.

Eigenvalues		
$\lambda_1 = -21.8 + 2004j$	$\lambda_7 = 16 - 392j$	$\lambda_{13} = -7.1$
$\lambda_2 = -21.8 - 2004j$	$\lambda_8 = -55 + 372j$	$\lambda_{14} = 8.77$
$\lambda_3 = -30.2 + 1252j$	$\lambda_9 = -55.3 - 372j$	$\lambda_{15} = -95$
$\lambda_4 = -30.2 - 1252j$	$\lambda_{10} = -33.7 + 121j$	$\lambda_{16} = 8.77$
$\lambda_5 = -490.8$	$\lambda_{11} = -33.7 - 121j$	$\lambda_{17} = -100$
$\lambda_6 = 16 + 392j$	$\lambda_{12} = -183.7$	$\lambda_{18} = -100$



**Figure 8.** Spectrum of the torus solution.

To observe the relationship between the gains  $D_p$  and  $D_q$  and the stability of the system, a double-parameter bifurcation analysis is performed. Figure 9 exhibits the bifurcation diagram between the gains  $D_p$  and  $D_q$ , where the blue curve corresponds to the limits of the SHB of the case study. The proposed system becomes unstable by reducing  $D_p$  or  $D_q$ , and this result is expected since by reducing these parameters, less reactive and active power is injected against frequency and voltage variations. It can also be seen that the bifurcation behavior is almost linear, except for  $D_p < 10$  (approximately). This means that the constants  $D_p$  and  $D_q$  hardly depend on each other, which is desired because the selection of these gains can be selected independently since they are practically decoupled. These limits depend on the system parameter and operating points. Figure 9 also shows that the value of  $D_q < 601.1$  leads to an unstable solution no matter the value of  $D_p$ . If lower values of this gain are needed to reach specific transient response or power management criteria, this system with the current set of control system parameters will be unstable; however, some other parameters, such as time constants  $\tau_f$  or  $\tau_v$ , can be varied to reach stable solutions.

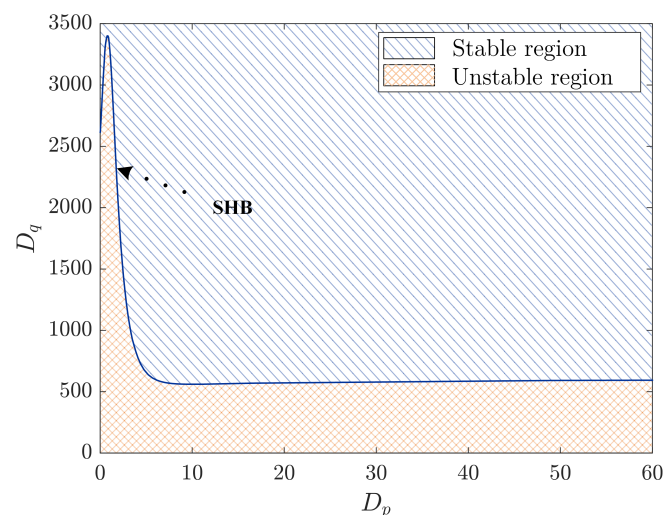


**Figure 9.** Stability region, when the gains vary  $D_q$ – $D_p$ , with  $\tau_f = 0.002$  s y  $\tau_v = 0.02$  s.

The impact of the time constants  $\tau_f$  and  $\tau_v$  on the stability region is shown in Figures 10 and 11, respectively. The results show that, by increasing the time constant  $\tau_f$  to 0.02 s, there is a small reduction in the stability region; however, the gained stability region evidence a linear boundary. This means that the gains  $D_p$  and  $D_q$  are decoupled from each other. When increasing this gain, it is not possible to appreciate any change in stability. In addition, the results show that by increasing the constant  $\tau_v$  to 2 s, the unstable regions

practically disappear for positive values of  $D_p$  and  $D_q$ . This means that for any positive value of the virtual inertia  $J$ , the system is stable since it depends on  $D_p$  and  $\tau_f$ . This is a strong result of the synchronverter proposed by [1], even with the highly nonlinear loads of the test system, which establishes that all positive values of these droop gains make the system stable for this set of parameters.

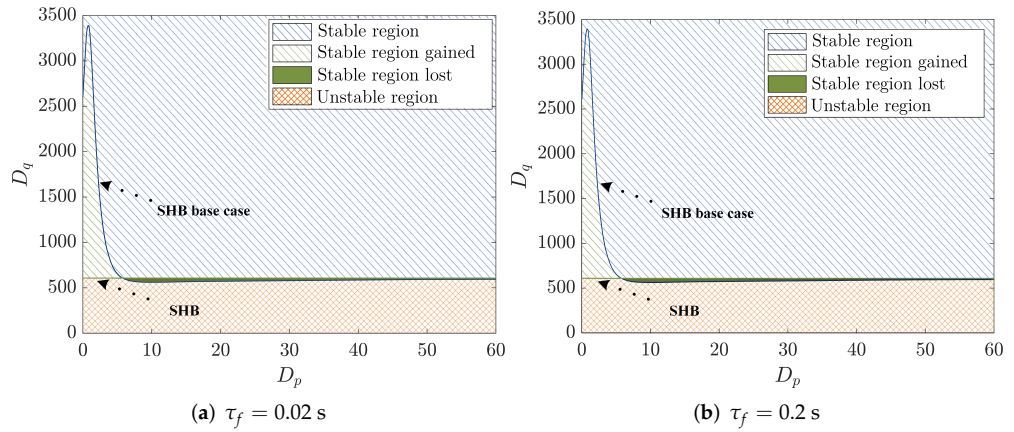


Figure 10. Region of stability of the plane  $D_q$ - $D_p$  before different values of  $\tau_f$ .

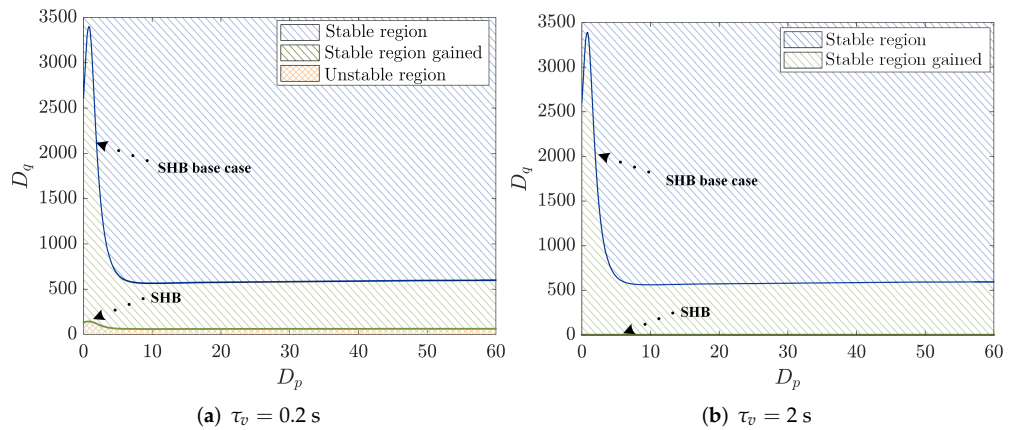


Figure 11. Region of stability of the plane  $D_q$ - $D_p$  for different values of  $\tau_v$ .

### 3.1.2. Bifurcation Analysis Varying the Load ZIP+IM

Load level is one of the main parameters affecting the stability; therefore, in this subsection, a bifurcation analysis is performed by varying the parameter  $P_0$ . As mentioned above, the effect of reactive power  $Q_0$  is implicit because of the power factor. The influence of load type, power factor, and control parameters are also investigated.

The bifurcation diagram that was obtained by varying the active power  $P_0$  for the different loads is shown in Figure 12. For the constant impedance load, a supercritical Hopf bifurcation (SUHB) occurs when  $P_0 = 1.243$  p.u. In the constant current load, a subcritical Hopf bifurcation (UHB) can be observed when  $P_0 = 2.248$  p.u., while for the constant power load, a saddle-node bifurcation (SNB) arises with the active power  $P_0 = 3.796$  p.u. Here, the three load types of the ZIP model present different bifurcations, and therefore, all three have a significant effect on the stability of the system.

The ZIP load and the ZIP+IM load present a UHB, but with the ZIP+IM load, this appears in a higher value, thus increasing the stability region; however, the operating limit (OL) is presented at a lower value, as shown in Figure 13. Focusing on the ZIP+IM load, the UHB branch appears at  $P_0 = 3.83$  p.u., and Figure 14 presents the periodic solutions that arise because of this bifurcation.

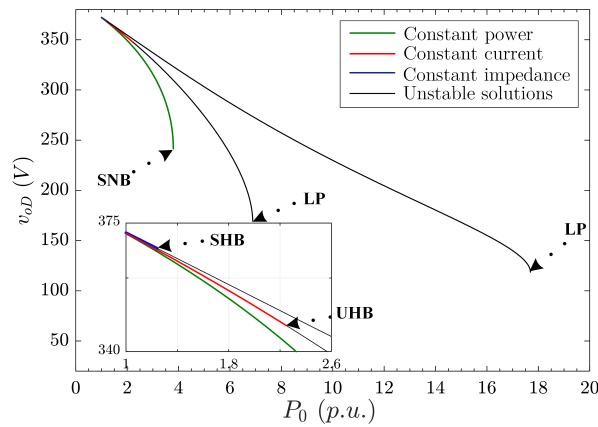


Figure 12. Bifurcation diagram for the different types of ZIP load models.

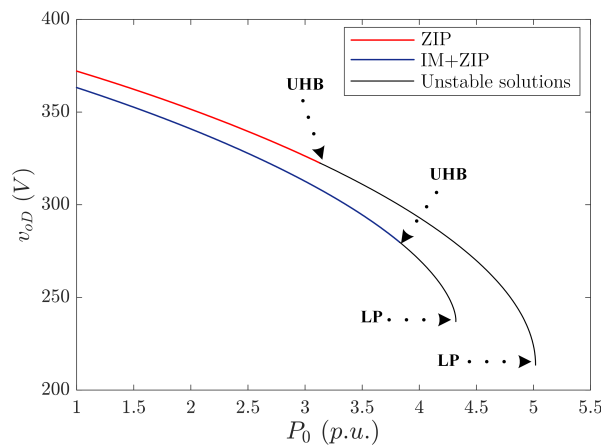


Figure 13. Bifurcation diagrams for the ZIP and ZIP+IM models.

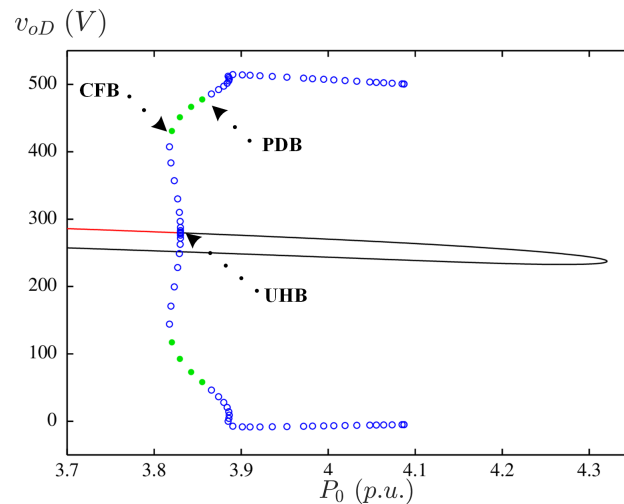


Figure 14. Bifurcation diagram when varying  $P_0$ : in red are the stable solutions, in black are the unstable solutions, in green are the stable periodic solutions, and in blue are the unstable periodic solutions.

If the system is oscillating in this stable limit cycle again, but now the bifurcation parameter is increased, a period-doubling bifurcation (PDB) occurs, which changes the initial stable orbit by two orbits. The behavior of this bifurcation is shown in Figure 15 for a value of  $P_0 = 3.86$  p.u.

By increasing the active power a little more than  $P_0 = 3.864$  p.u., the system experiences a TRB, causing its variables to oscillate with two frequencies.

If the active power increases, for example, at  $P_0 = 3.89$  p.u., the system will go from having two oscillations of constant amplitude to presenting oscillations of increasing amplitude. Therefore, the angle between the load and the synchronverter increases, usually causing voltage collapse or loss of synchronization before reaching the maximum loadability point. However, as seen in Figure 16, although the system presents a loss of synchronism because of the increasing angle  $\delta$ , the other variables present constant oscillations. This dynamic in the  $abc$  frame is observed as oscillations with two frequencies, as seen in Figure 17.

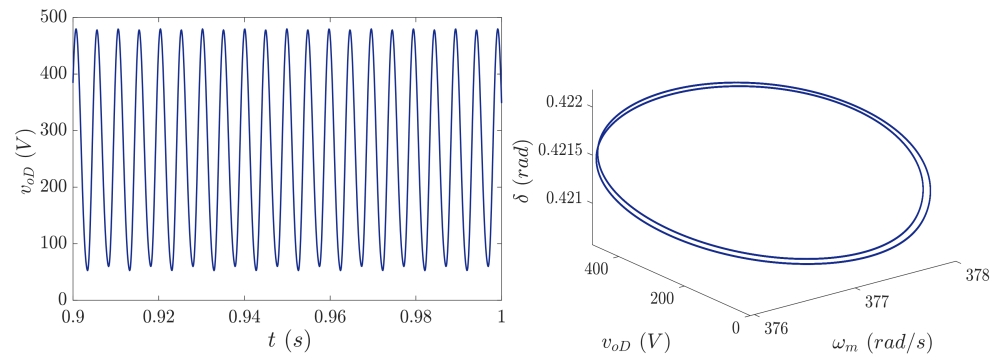


Figure 15. Period-doubling oscillations at  $P_0 = 3.86$  p.u.

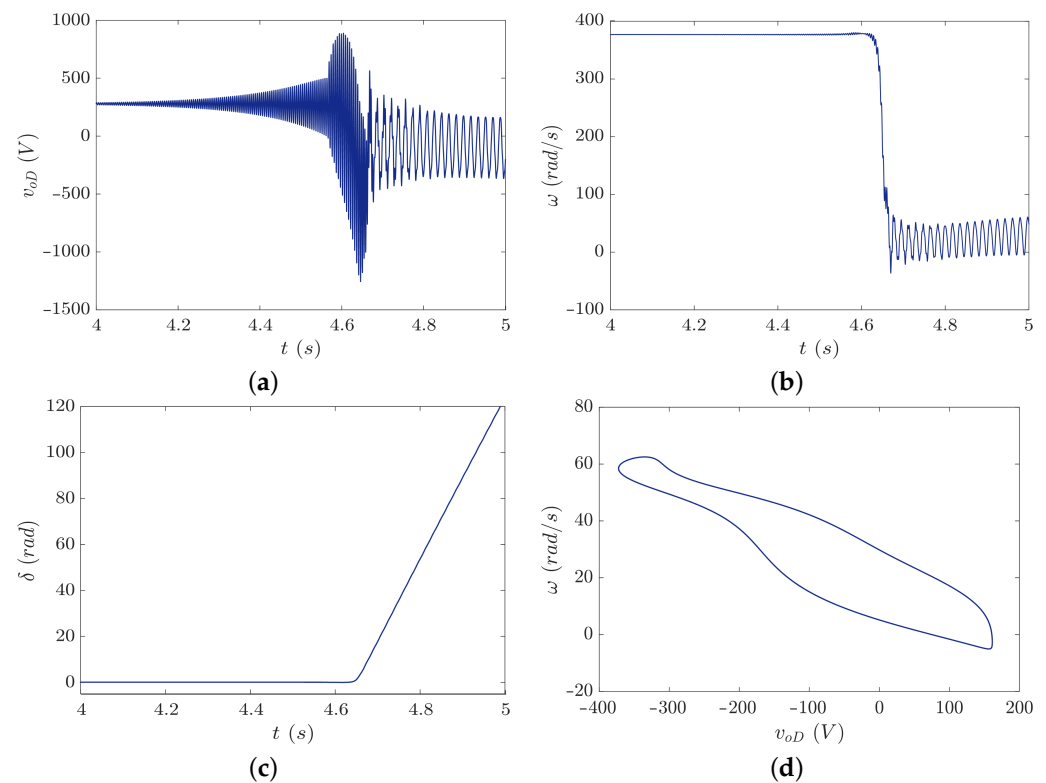
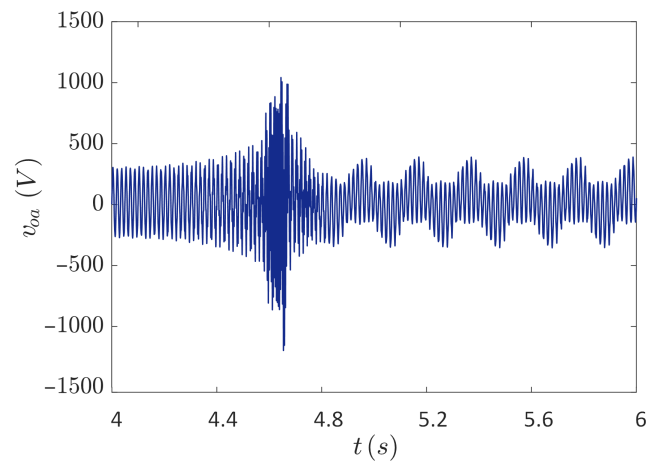


Figure 16. The behavior of the system when the loss of synchronism occurs at  $P_0 = 3.89$  p.u.: (a–c) Time response of the voltage, angular velocity, and angle. (d) Steady-state phase portrait.

The appearance of the Hopf bifurcation can be controlled either by varying the gain  $D_q$  or the power factor ( $PF$ ); this can be seen in Figure 18. For the first case, when the gain  $D_q$  is decreased, the subcritical Hopf branch tends to disappear; however, the stable regions are reduced. On the contrary, when the gain  $D_q$  increases, the Hopf bifurcation appears at a higher value, thus increasing the stable regions. Increasing the gain  $D_q$  implies that the system must inject more reactive power in the event of minor voltage variations.

Therefore, this way of controlling the bifurcations is not very effective, so a balance must be found between the desired stable region and the maximum reactive power available by the synchronverter.



**Figure 17.** Voltage response on *abc* in  $P_0 = 3.89$  p.u.

By varying the power factor, the results show that by having  $PF > 0.755$  (lagging), the UHB disappears and the OL increases, so this second form of controlling the Hopf branch is a more practical option.

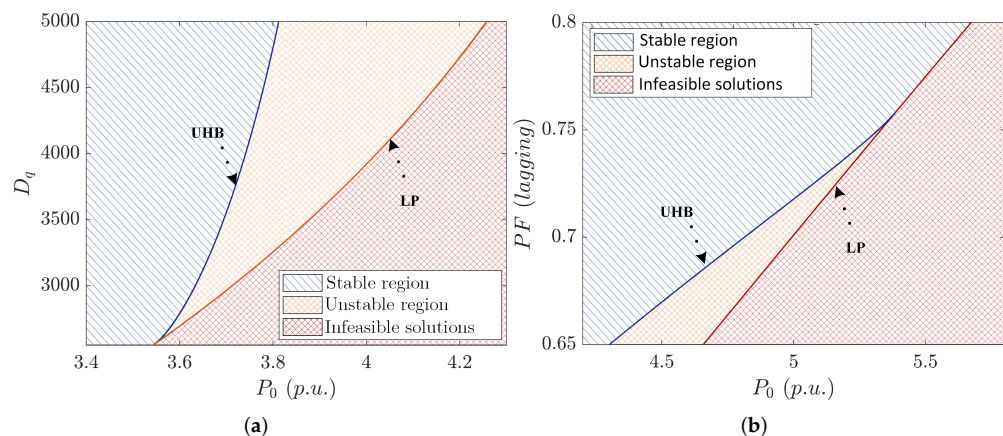


**Figure 18.** Stability region when varying: (a) The control gain  $D_q$ . (b) The power factor  $PF$ .

### 3.1.3. Bifurcation Analysis at the Thévenin Equivalent

The Thévenin equivalent is constantly changing because of the constant connection and disconnection of elements, loads, and generation, as well as the varying load demand and generation. The circuit equivalent of the grid is commonly given in terms of its short-circuit capacity, the nominal voltage, the X/R relation, and implicitly, the nominal grid frequency. These four data comply with the Thévenin equivalent made up of an equivalent voltage source in series with an RL branch. The relationship between the SCC and the injected or demanded power across the PCC is known as a short-circuit ratio (SCR). Low SCR values refer to weak systems, and high values refer to stiff systems. Regarding the stability of grid-connected inverters, weak systems are more susceptible to losing stability. To assess the impact of the grid equivalent on the stability of the synchronverter, the stability region in the  $L_g - R_g$  plane is computed, as well as the bifurcation diagram with  $L_g$  as the bifurcation parameter.

The inductance  $L_g$  varies, and the resulting bifurcation diagram is shown in Figure 19. It can be seen that an SNB appears in the OL at  $L_g = 25.41$  mH. This value is very far from the initial value of  $L_g = 0.565$  mH, which indicates a relatively large stability

margin for  $L_g$ . Notice that the apparition of the SNB is just on the turning point of the bifurcation diagram, which indicates that the stability limit overlaps the feasible solution, i.e., operatively, it is the best performance in that all the values of  $L_g$  make the system stable.

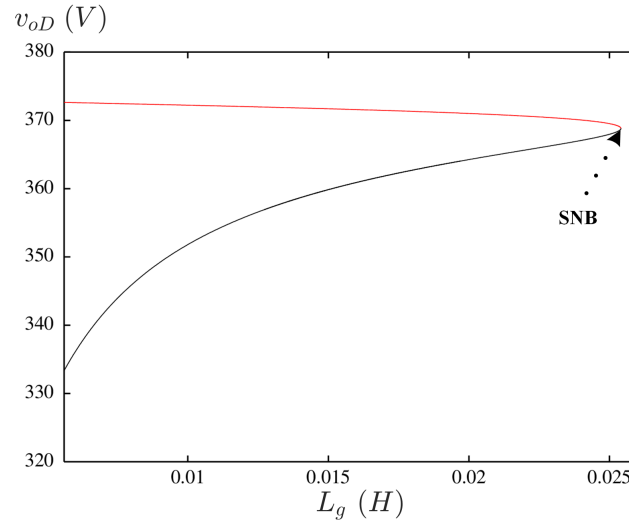


Figure 19. Bifurcation diagram by varying  $L_g$ : stable solutions in red and unstable solutions in black.

Figure 20 shows the stability region at the  $L_g - R_g$  plane at different values of the voltage magnitude of the Thévenin equivalent  $V_g$  (the magnitude of the line-to-line voltage in RMS), where the base case is a  $V_g = 460 V$ . It can be seen that the system does not present feasible solutions for large values of  $R_g$  and  $L_g$ . Furthermore, it can be observed that by increasing the voltage of the network  $V_g$ , the region of stability increases. The results obtained in Figure 20 are consistent with the fact that the reduction in the short-circuit capacity (weak systems) leads to less stable systems. Although the stability of the electrical system is lost with large values of network inductance and capacitance, these values correspond to short-circuit capacities well below the nominal power of the PCC and therefore are values that in a practical system could not be reached. This means that the stability of the synchronverter is robust to changes in the Thévenin equivalent. Notice that the stability boundary is limited by SNB, which is a more dangerous loss of stability compared with the SHB or the UHB since the SNB makes the variables grow suddenly. Fortunately, it is not something to worry about in this case, since these limits correspond to very low levels of SCR, which makes them unrealistic in practical systems.

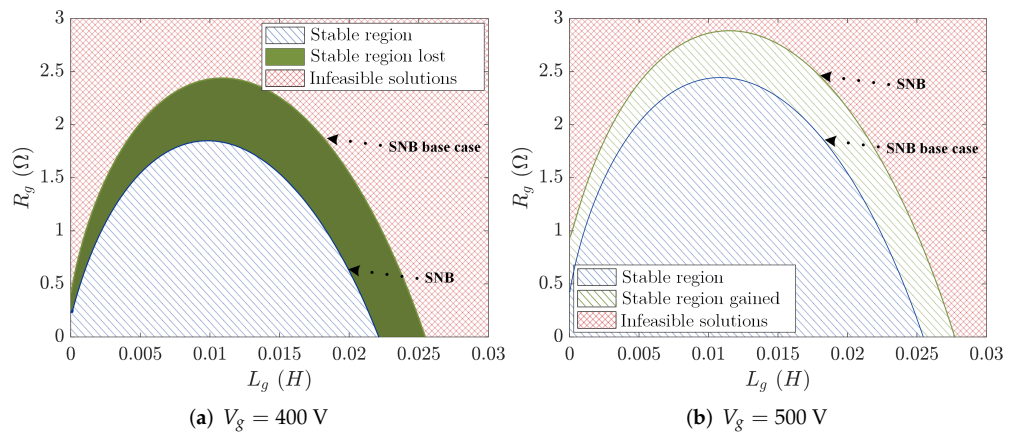


Figure 20. Stability region in  $L_g - R_g$  plane for different Thévenin voltages  $V_g$ .

#### 4. Conclusions

In this paper, a bifurcation analysis was carried out to determine how synchronverter parameters variation affects the system stability. We can conclude that:

1. A reduction in the droop gain  $D_p$  or the time constant  $t_f$  leads to a reduction in the synchronverter inertia, which causes the system to present Hopf bifurcations, making the system susceptible to showing oscillations.
2. The increase in the time constants  $t_f$  or  $t_v$  allows the decoupling of the active power loop and the reactive power loop, which is important in the synchronverter parameters selection. Furthermore, the increase in the time constant  $t_v$  allows for improving the stability region on the  $D_p - D_q$  plane.
3. The increase in the droop gain  $D_q$  or of the power factor  $PF$  allows for an increase in the system OL.
4. In general, large values of  $R_g$  and  $L_g$  and low voltage magnitude ( $V_g$ ) lead to a less stable system.

Some future works aim to extend this analysis to microgrids, islanded and connected to the grid, with multiple synchronverters, linear and nonlinear loads, battery storage systems, and other types of power electronic inverter controls for the integration of renewable energies.

**Author Contributions:** Conceptualization, J.S.R., J.H.R., N.V.C. and R.P.G.; methodology, J.S.R. and J.H.R.; software, J.H.R.; validation, J.S.R., J.H.R. and N.V.C.; formal analysis, J.S.R., J.H.R., N.V.C. and R.P.G.; investigation, J.S.R. and J.H.R.; resources, J.S.R. and J.H.R.; data curation, J.H.R.; writing—original draft preparation, J.S.R. and R.P.G.; writing—review and editing, J.S.R. and R.P.G.; visualization, J.S.R. and J.H.R.; supervision, J.S.R., N.V.C. and R.P.G.; project administration, J.S.R.; funding acquisition, J.S.R. All authors have read and agreed to the published version of the manuscript.

**Funding:** This research was funded by the FORDECYT-PRONACES, grant number 1311344/2020.

**Institutional Review Board Statement:** Not applicable.

**Informed Consent Statement:** Not applicable.

**Data Availability Statement:** Not applicable.

**Acknowledgments:** The authors want to acknowledge the Universidad Autónoma de San Luis Potosí for the facilities granted to carry out this research. Josué Hernández Ramírez thanks the financial support received from CONACYT with the scholarship 746757 to carry out his studies.

**Conflicts of Interest:** The authors declare no conflict of interest. The funders had no role in the design of the study; in the collection, analyses, or interpretation of data; in the writing of the manuscript; or in the decision to publish the results.

#### Abbreviations

The following abbreviations are used in this manuscript:

DQ	direct-quadrature reference frame
IM	induction motor
OL	operating limit
PCC	point of common coupling
PDB	period-doubling bifurcation
PF	power factor
RLC	resistive-inductive-capacitive
RMS	root mean square
SCC	short-circuit current
SCR	short-circuit ratio
SG	synchronous generators
SHB	supercritical Hopf bifurcation
SNB	saddle-node bifurcation
SHB	stable Hopf bifurcation

SUHB	Supercritical Hopf bifurcation
TRB	Torus bifurcation
UHB	Subcritical Hopf bifurcation
VSC	Voltage source converters
VSG	Virtual synchronous generators

## Nomenclature

$\delta$	Angle between the frame $dq$ and the common frame of reference $DQ$ .
$e_D, e_Q$	Voltage at inverter terminals (D and Q axis).
$e$	Voltage at inverter terminals.
$M_f i_f$	Excitation of the imaginary field.
$J$	Virtual moment of inertia of the synchronverter.
$D_p$	Frequency-drooping coefficient.
$D_q$	Voltage-drooping coefficient.
$T_e$	Electromagnetic torque of the synchronverter.
$T_{mm}$	Electromagnetic torque of the motor.
$\theta$	Angle of the synchronverter.
$\omega$	Angular frequency of the synchronverter.
$\omega_m$	Angular velocity of the rotor.
$\omega_{em}$	Electrical angular velocity of the motor.
$\omega_{grid}$	Angular frequency of the grid.
$\omega^*$	Reference angular frequency.
$P$	Active power.
$Q$	Reactive power.
$P_{ZIP}$	Active power of the ZIP load.
$Q_{ZIP}$	Reactive power of the ZIP load.
$G_{ZIP}$	Conductance of the ZIP load.
$B_{ZIP}$	Susceptance of the ZIP load.
$P^*$	Reference active power.
$Q^*$	Reference reactive power.
$K$	Coefficient of inertia related to the gain $Dq$ .
$\tau_f$	Time constant of the frequency droop loop.
$\tau_v$	Time constant of the voltage droop loop.
$i_L$	Synchronverter output current.
$i_{LD}, i_{LQ}$	Synchronverter output current (D and Q axis).
$v_{oD}, v_{oQ}$	Synchronverter output voltage (D and Q axis).
$i_{gD}, i_{gQ}$	Grid output current (D and Q axis).
$v_{gD}, v_{gQ}$	Grid output voltage (D and Q axis).
$\psi_{sD}, \psi_{sQ}$	Flux links of stator windings (D and Q axis).
$\psi_{rD}, \psi_{rQ}$	Flux links of rotor windings (D and Q axis).
$i_{pD}, i_{pQ}$	Conductance output current (D and Q axis).
$i_{qD}, i_{qQ}$	Susceptance output current (D and Q axis).
$v^*$	Amplitude of the reference voltage.
$v_m$	Amplitude of the synchronverter output voltage.
$V_p$	Amplitude of the grid voltage.
$p$	Number of pole pairs.
$L_{sm}$	Stator inductance.
$R_{sm}$	Stator resistance.
$L_r$	Rotor inductance.
$R_r$	Rotor resistance.
$L_m$	Magnetization inductance.
$J_m$	Virtual moment of inertia of the motor.
$D_m$	Damping constant.
$C$	Capacitor.
$L_g$	Grid inductance.
$R_g$	Grid resistance.
$L_s$	Synchronverter inductance.

$R_s$	Synchronverter resistance.
$P_0$	Reference active power of the ZIP load.
$Q_0$	Reference reactive power of the ZIP load.
$a_1, b_1$	Percentages of the constant-impedance load.
$a_2, b_2$	Percentages of the constant-current load.
$a_3, b_3$	Percentages of the constant-power load.
$PF$	Power factor.
$\tau$	Time constant of the ZIP load.
$U_0$	Nominal magnitude voltage of the ZIP load.
$U_b$	Actual voltage magnitude of the ZIP load.
$\omega_k$	Angular frequency of the component to refer.

## References

- Zhong, Q.C.; Weiss, G. Synchronverters: Inverters That Mimic Synchronous Generators. *IEEE Trans. Ind. Electron.* **2011**, *58*, 1259–1267. [\[CrossRef\]](#)
- Zhong, Q.C. Virtual Synchronous Machines: A unified interface for grid integration. *IEEE Power Electron. Mag.* **2016**, *3*, 18–27. [\[CrossRef\]](#)
- Tamrakar, U.; Shrestha, D.; Maharjan, M.; Bhattarai, B.P.; Hansen, T.M.; Tonkoski, R. Virtual Inertia: Current Trends and Future Directions. *Appl. Sci.* **2017**, *7*, 654. [\[CrossRef\]](#)
- Wu, H.; Ruan, X.; Yang, D.; Chen, X.; Zhao, W.; Lv, Z.; Zhong, Q.C. Small-Signal Modeling and Parameters Design for Virtual Synchronous Generators. *IEEE Trans. Ind. Electron.* **2016**, *63*, 4292–4303. [\[CrossRef\]](#)
- Vetoshkin, L.; Müller, Z. A comparative analysis of a power system stability with virtual inertia. *Energies* **2021**, *14*, 3277. [\[CrossRef\]](#)
- Chen, M.; Zhou, D.; Blaabjerg, F. Modelling, Implementation, and Assessment of Virtual Synchronous Generator in Power Systems. *J. Mod. Power Syst. Clean Energy* **2020**, *8*, 399–411. [\[CrossRef\]](#)
- Rosso, R.; Engelken, S.; Liserre, M. Robust stability analysis of synchronverters operating in parallel. *IEEE Trans. Power Electron.* **2019**, *34*, 11309–11319. [\[CrossRef\]](#)
- Ebrahimi, H.; Yazdaninejadi, A.; Golshannavaz, S. Transient stability enhancement in multiple-microgrid networks by cloud energy storage system alongside considering protection system limitations. *IET Gener. Transm. Distrib.* **2022**. [\[CrossRef\]](#)
- Shuai, Z.; Hu, Y.; Peng, Y.; Tu, C.; Shen, Z.J. Dynamic stability analysis of synchronverter-dominated microgrid based on bifurcation theory. *IEEE Trans. Ind. Electron.* **2017**, *64*, 7467–7477. [\[CrossRef\]](#)
- Shuai, Z.; Peng, Y.; Liu, X.; Li, Z.; Guerrero, J.M.; Shen, Z.J. Parameter Stability Region Analysis of Islanded Microgrid Based on Bifurcation Theory. *IEEE Trans. Smart Grid* **2019**, *10*, 6580–6591. [\[CrossRef\]](#)
- Segundo-Ramirez, J.; Medina, A.; Ghosh, A.; Ledwich, G. Stability analysis based on bifurcation theory of the DSTATCOM operating in current control mode. *IEEE Trans. Power Deliv.* **2009**, *24*, 1670–1678. [\[CrossRef\]](#)
- Amin, M.; Rygg, A.; Molinas, M. Self-Synchronization of Wind Farm in an MMC-Based HVDC System: A Stability Investigation. *IEEE Trans. Energy Convers.* **2017**, *32*, 458–470. [\[CrossRef\]](#)
- Ray, I. Review of impedance-based analysis methods applied to grid-forming inverters in inverter-dominated grids. *Energies* **2021**, *14*, 2686. [\[CrossRef\]](#)
- Strogatz, S.H. *Nonlinear Dynamics and Chaos: With Applications to Physics, Biology, Chemistry, and Engineering*; CRC Press: Boca Raton, FL, USA, 2018.
- Vasudevan, K.R.; Ramachandramurthy, V.K.; Babu, T.S.; Pouryekt, A. Synchronverter: A Comprehensive Review of Modifications, Stability Assessment, Applications and Future Perspectives. *IEEE Access* **2020**, *8*, 131565–131589. [\[CrossRef\]](#)
- Sonawane, A.J.; Umarikar, A.C. Small-Signal Stability Analysis of PV-Based Synchronverter Including PV Operating Modes and DC-Link Voltage Controller. *IEEE Trans. Ind. Electron.* **2022**, *69*, 8028–8039. [\[CrossRef\]](#)
- Rodríguez-Cabero, A.; Roldan-Perez, J.; Prodanovic, M. Synchronverter small-signal modelling and eigenvalue analysis for battery systems integration. In Proceedings of the 2017 IEEE 6th International Conference on Renewable Energy Research and Applications (ICRERA), San Diego, CA, USA, 5–8 November 2017; pp. 780–784. [\[CrossRef\]](#)
- Rosso, R.; Cassoli, J.; Buticchi, G.; Engelken, S.; Liserre, M. Robust Stability Analysis of LCL Filter Based Synchronverter Under Different Grid Conditions. *IEEE Trans. Power Electron.* **2019**, *34*, 5842–5853. [\[CrossRef\]](#)
- Chiang, H.D.; Dobson, I.; Thomas, R.; Thorp, J.; Fekih-Ahmed, L. On voltage collapse in electric power systems. *IEEE Trans. Power Syst.* **1990**, *5*, 601–611. [\[CrossRef\]](#)
- Agundis-Tinajero, G.D.; Vasquez, J.C.; Guerrero, J.M. Stability Boundary Analysis of Islanded Droop-Based Microgrids Using an Autonomous Shooting Method. *Energies* **2022**, *15*, 2120. [\[CrossRef\]](#)
- Doedel, E.; Paffenroth, R.; Champneys, A.; Fairgrieve, T.; Kuznetsov, Y.A.; Oldeman, B.; Sandstede, B.; Wang, X. *AUTO 2000: Continuation and Bifurcation Software for Ordinary Differential Equations (with HomCont)*; California Institute of Technology: Pasadena, CA, USA, 2002.
- Gao, F.; Iravani, M.R. A Control Strategy for a Distributed Generation Unit in Grid-Connected and Autonomous Modes of Operation. *IEEE Trans. Power Deliv.* **2008**, *23*, 850–859. [\[CrossRef\]](#)

23. Udrill, J.M. Dynamic Stability Calculations for an Arbitrary Number of Interconnected Synchronous Machines. *IEEE Trans. Power Appar. Syst.* **1968**, *PAS-87*, 835–844. [[CrossRef](#)]
24. Peña, R.; Medina, A. Fast steady-state parallel solution of the induction machine. In Proceedings of the XIX International Conference on Electrical Machines-ICEM 2010, Rome, Italy, 6–8 September 2010; pp. 1–5.
25. Krause, P.C.; Wasynczuk, O.; Sudhoff, S.D.; Pekarek, S.D. *Analysis of Electric Machinery and Drive Systems*; John Wiley & Sons: Hoboken, NJ, USA, 2013; Volume 75.
26. Milanovic, J.V.; Yamashita, K.; Martínez Villanueva, S.; Djokic, S.Z.; Korunović, L.M. International Industry Practice on Power System Load Modeling. *IEEE Trans. Power Syst.* **2013**, *28*, 3038–3046. [[CrossRef](#)]